Available online at www.sciencedirect.com
SCIENCE DIRECT®
ELSEVIER
Nuclear Instruments and Methods in Physics Research B 217 (2004) 262–275
NIM B
Beam Interactions with Materials & Atoms
www.elsevier.com/locate/nimb

Protrusion formation and surface porosity development on thermally annealed helium implanted copper

R. Escobar Galindo [a,*], A. van Veen [a], J.H. Evans [b], H. Schut [a], J.Th.M. de Hosson [c]

[a] *Interfaculty Reactor Institute, Delft University of Technology, Mekelweg 15, NL-2629 JB Delft, The Netherlands*
[b] *27 Clevelands, Abingdon OX14 2EQ, UK*
[c] *Materials Science Centre and NIMR, University of Groningen, Nijenborgh 4, NL-9747 AG Groningen, The Netherlands*

Received 27 December 2002; received in revised form 24 September 2003

Abstract

Surface effects on (1 1 1) copper single crystal surfaces after 30 keV helium implantation up to 2.4×10^{16} ions cm^{-2} and subsequent annealing at 973 K have been studied using scanning electron and confocal microscopy. Since one aim of the work was to develop a method of studying the adhesion of surface coatings, the implantations were performed both directly and through periodical microsieves with pore sizes of 1.5 and 4.5 μm. Different behaviour was observed depending on the sample area studied. Of particular interest was the appearance of surface protrusions in directly implanted areas for all implantation doses, with faceted spheroids above 1.8×10^{16} ion cm^{-2}. These spheroids increase in number with dose and have sizes of 1–2 μm with distinguishable {1 1 1} and {1 0 0} facets, in agreement with the Wulff diagram.

The implantation through the periodical microsieve with 4.5 μm pore size resulted in clear periodical patches reflecting the escape of helium from these areas. However, decreasing the pore size to 1.5 μm broke the periodical pattern. The results have been interpreted in terms of bubble migration, coalescence and swelling.

1. Introduction

The use of coatings on materials and in thin films systems is well known with numerous applications. In this field considerable attention has been paid to reliable ways of measuring the adhesion of coatings to substrates. One standard test has been the blister test originally proposed by Dannenberg involving the injection of a liquid between substrate and coating in such a way that the coating is detached in form of a blister [1]. Williams [2] introduced the blister test as we know it now and applied it to measure the fracture energy of thin coatings on rigid substrates. A constrained blister geometry was introduced by Napolitano et al. [3] to avoid uncontrolled growth of the blister at the liquid or gas pressure, and was analyzed, among others, by Lai and Dillard [4,5].

* Corresponding author. Present address: Departamento de Fisica e Ingeniería de Superficies, Instituto de Ciencia de Materiales de Madrid, Consejo Superior de Investigaciones Científicas, Cantoblanco, 28049 Madrid, Spain. Tel.: +91-372-14-20; fax: +91-372-06-23, +31-15-278-6422.
E-mail address: rescobar@icmm.csic.es (R. Escobar Galindo).

0168-583X/$ - see front matter © 2003 Elsevier B.V. All rights reserved.
doi:10.1016/j.nimb.2003.10.012

Borisenko et al. [6] have shown a correlation between gas blister parameters and the adhesion properties of hydrogen implanted thin silver films on glass substrates.

Against this background, the present work has examined the possibility of using gas release from substrates previously implanted with helium to develop blister formation between the substrate and a subsequently deposited thin film. During helium implantation into metals at ambient temperature, it is well known that the helium is trapped at the implant depth in implantation induced vacancies at low doses [7] and forms small bubbles [8] at higher doses. Annealing of such material leads to a clear surface release of the helium, as individual atoms at low doses, while in samples containing bubbles, bubble migration leads to coalescence of the bubbles, bubble swelling and the loss of bubbles at nearby surfaces. For helium in copper, Johnson and Mazey [9] have reported transmission electron microscopy observations showing such bubble behaviour starting at near $0.44T_m$ (598 K) while in analogous work in copper containing krypton bubbles [10] there were clear surface effects consistent with the arrival of bubbles and the associated release of gas. For the helium case the presence of a surface coating would lead to the agglomeration of the implanted gas at the film–metal interface during annealing and thus to interface blister formation. An increase in the blister pressure in a controlled way would then induce delamination as described above.

These interface blisters must not be confused with the surface blistering that occurs on uncoated metal surfaces at high helium doses [11] during ambient temperature implantation. This blister formation requires a peak helium content of ~30 at.%. In the present work the chosen helium levels are some 15–30 times lower, but these levels will be sufficient to investigate the expected annealing induced loss of bubbles to the surface that might be relevant to interface blister effects if samples were coated. Besides examining directly implanted surfaces after annealing, a novel approach in this work has been to implant the copper through periodic microsieves as a method of controlling the initial blister size in coated samples. The present study focuses on helium implanted copper samples without any coating deposited. On the basis of the results we explain the mechanism of helium bubble growth and swelling that causes the creation of blisters at the copper surface after annealing.

2. Experimental

Cu(1 1 1) crystals were polished down to a roughness of 1 μm and annealed at 873 K for 30 min under a vacuum of about 10^{-5} Pa. 30 keV ^{4}He and ^{3}He ion implantations were performed using a VARIAN 350D and a DANFYSIK ion implanter, respectively.

The implantations were performed through a periodical microsieve provided by AquaMarijn (Fig. 1). Two different pore sizes were used for the implantations: 1.5 and 4.5 μm. The distance between the centre of neighbour pores is twice the pore size. As the microsieve partly covered the samples, two implantation zones were considered. These will be referred hereafter as the direct implantation area and microsieve implantation area, respectively. Three different fluences were applied: 1.2, 1.8 and 2.4×10^{16} ions cm^{-2} measured by neutron depth profiling (NDP) [12] with a typical error of 7×10^{13} ions cm^{-2}. The implantation range was 130 ± 57 nm according to TRIM [13] giving approximate peak concentrations of 0.83, 1.25 and 1.68 at.%, respectively, as can be seen in Fig. 2. After implantation the samples were annealed at 973 K (0.72 times the melting

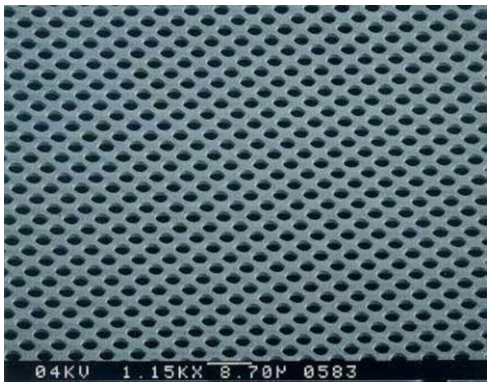

Fig. 1. SEM picture of AquaMarijn microsieve showing the periodical pattern.

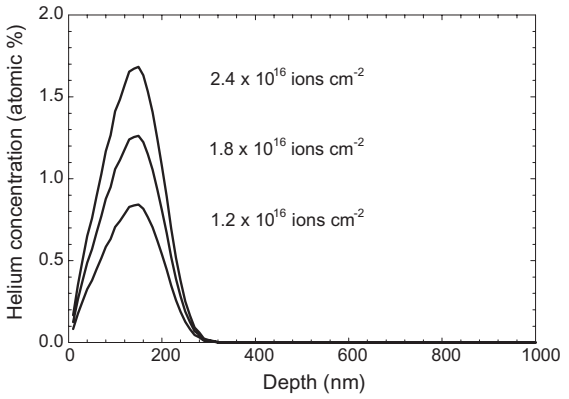

Fig. 2. Helium concentration in at.% calculated by TRIM for the implantation doses studied.

temperature T_m) for 30 min under a vacuum of about 10^{-5} Pa.

The observations and measurements of the blisters were performed using an Philips X30L Scanning Electron Microscope (SEM) and a μSurf Confocal Scanning Optical Microscope from Nanofocus Meßtechnique GmbH.

3. Results

After the implantation at RT for the above-mentioned doses, no signs of surface effects were seen on any samples. However, clear effects were seen after subsequent annealing at 973 K for 30 min with a variation depending on the implantation area studied. NDP experiments were performed after annealing revealing that 19% of the implanted helium remained in the samples. Details of the implantation areas will be given in turn.

3.1. Direct implantation area

After annealing, unusual surface protrusions were observed in this area for all doses. Representative SEM micrographs at low and high magnifications are shown in Fig. 3 for the three doses with additional micrographs for the medium dose after the surface had been electrochemically etched. The density of the protrusions increases with the fluences from 1 per 200 μm^2 for the lowest dose, up to 1 per 150 μm^2 for the 2.4×10^{16} ion cm^{-2} dose. At the lowest dose of 1.2×10^{16} ion cm^{-2} three-blade and elongated protrusions are predominant, Fig. 3(e). For higher fluences (1.8 and 2.4×10^{16} ion cm^{-2}) these are still present but in addition, non-cracked and faceted spheroids, Figs. 3(f) and (h), with {1 1 1} and {1 0 0} facets are seen. Examples of the different protrusion morphologies are also shown more clearly in Fig. 4.

The spheroids of the type seen in Fig. 4(a) have a height of approximately 2 μm and diameter of 1.4 μm for the 2.4×10^{16} ion cm^{-2} dose, as measured with the confocal microscope. This results in a typical volume of 3.2×10^{-12} cm^3 per protrusion with a wall thickness calculated to be about 30 nm. Electropolishing of the 1.8×10^{16} ion cm^{-2} sample shows the porous structure inside or underneath a spheroid (Fig. 3(g)). Three-blade blisters were also developed with a more pronounced faceted structure and cracks than for the low dose (Fig. 4(b)).

Apart from the formation of protrusions it can be observed in the SEM pictures in Figs. 3 and 4 that small black dots appear on the surface of the implanted copper after annealing. These dots indicate the bubbles through which the helium escapes from the sample and are similar to those seen on copper–krypton samples after annealing [10,14]. The size and concentration of the small dots were quantified applying a MATLAB program developed by van Tijum [15] to process images digitally. In Fig. 5 it is shown that the image processing of Fig. 3(e) results in a mean dot size of 144 ± 39 nm and an areal density of 3 dots per μm^2.

For the other implantation doses neither the size nor the concentration of dots were different. Other observations include the protrusion decoration of the scratches present before implantation and the surface roughness of the samples after implantation and subsequent annealing.

3.2. Microsieve implantation area

3.2.1. 1.5 μm microsieve

Representative micrographs on these areas are given in Fig. 6. At the lowest dose, (a) and (e), implantation and annealing led to the formation of

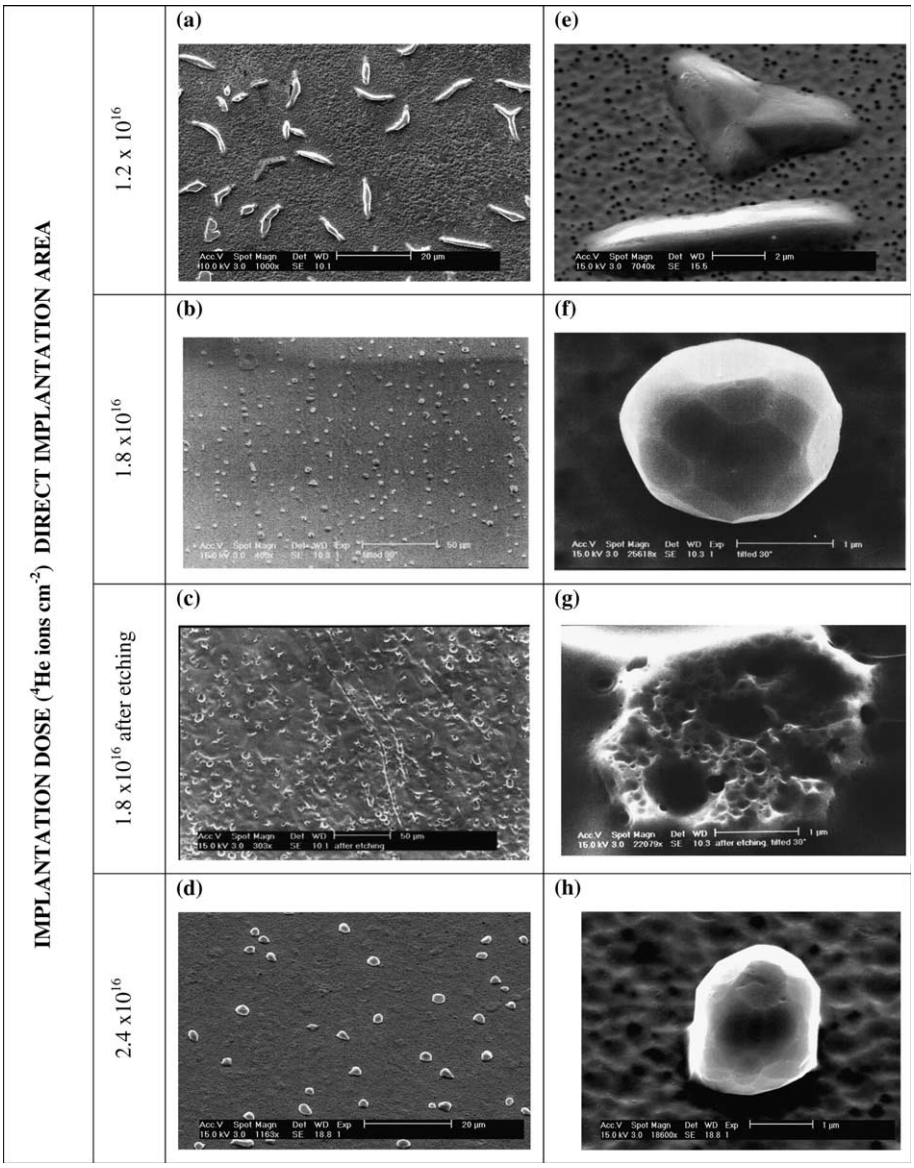

Fig. 3. Selection of SEM pictures obtained from the direct implantation area after implantation at 1.2×10^{16} (a, e), 1.8×10^{16} (b, f) and 2.4×10^{16} (d, h) He ions cm^{-2} and annealing. Pictures (c) and (g) were obtained after electrochemical etching of the sample implanted at 1.8×10^{16} He ions cm^{-2}.

small areas of low flat deformation suggesting subsurface swelling. After an increase of the dose, a few bigger protrusions (density 1 per 700 μm^2) developed on the surface, (b) and (f). At the highest dose of 2.4×10^{16} ion cm^{-2}, these have a typical diameter of about 3 μm, a height of approximately 0.5 μm and were open along their axes, (d) and (h). Electropolishing of the 1.8×10^{16} cm^{-2} sample revealed the presence of the implanted areas underneath (c) and (g). The pores are arranged in rows and a large distribution of sizes is observed. There are large pores with a

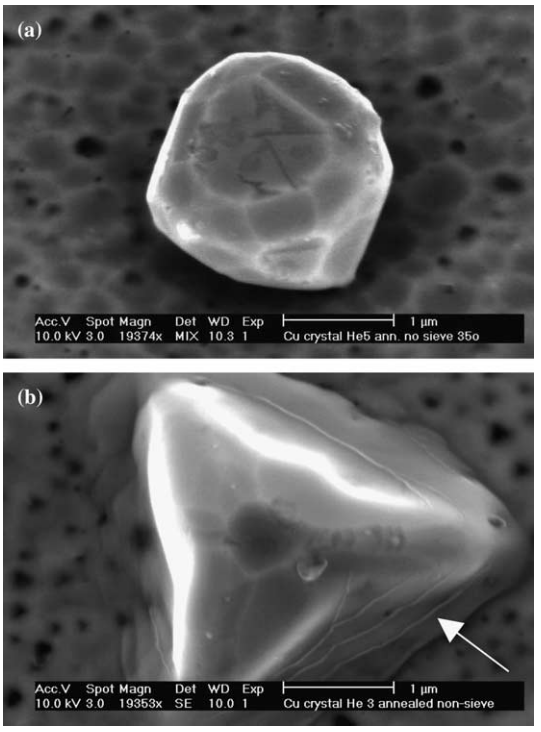

Fig. 4. Different types of blisters observed in the direct implantation area at the highest implantation dose of 2.4×10^{16} ions cm^{-2}: (a) a dome-shaped, faceted and non-broken blister; (b) three-blade, faceted and cracked blister (see white arrow).

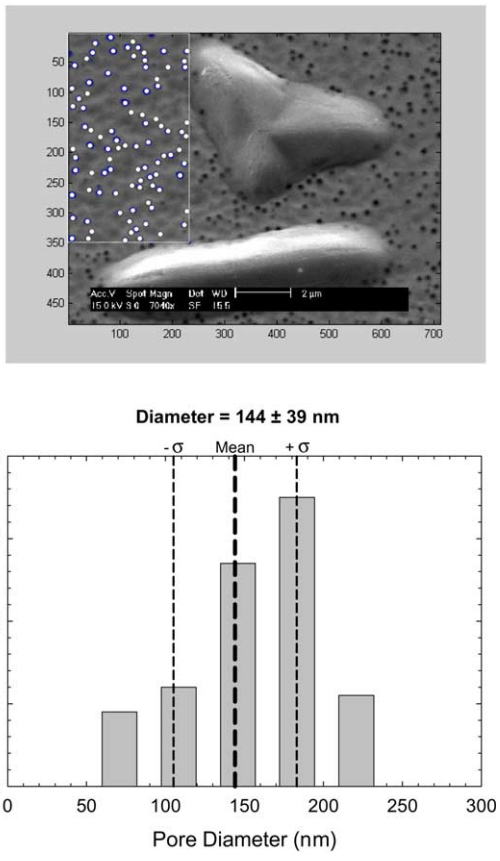

Fig. 5. Diameter distribution of small Helium bubbles (black dots) in the direct implantation area after 1.2×10^{16} He ions cm^{-2} implantation and annealing.

diameter of about 1.5 μm and small pores approximately 150 nm in size. The large pores are related to the periodical pattern of the microsieve and the small pores have similar size as the black dots observed in Figs. 3 and 4 (indicating the formation of bubbles). The biggest pore observed in Fig. 6(c) (with a diameter of about 3 μm) is related to the few protrusions detected in Fig. 6(b).

3.2.2. 4.5 μm microsieve

In contrast with the small pore size results, implantation through the 4.5 μm microsieve resulted in a periodical pattern of patches for all doses studied, as can be seen in Fig. 7.

These patches reproduce the periodical pattern of the microsieve. They are homogeneous in shape (circular) and size (4.5 μm), and are essentially identical to each other. There is no development of large protrusions but instead the surfaces are characterized by some roughness and the small helium release pores discussed previously. Results of pore size measurement are given in Fig. 8 with a mean size of 156 ± 82 nm and a concentration of ~3 per μm^2 for the highest dose (Fig. 7(h)). There is no indication of gas release in the surface area between the periodical patches.

To conclude this section, the main results are summarized in Table 1.

4. Discussion

In the context of using the present approach to control interface blister formation (see Section 1), perhaps the most important result was the appearance of the identical periodic patches found in the 4.5 μm microsieve results. However, it is

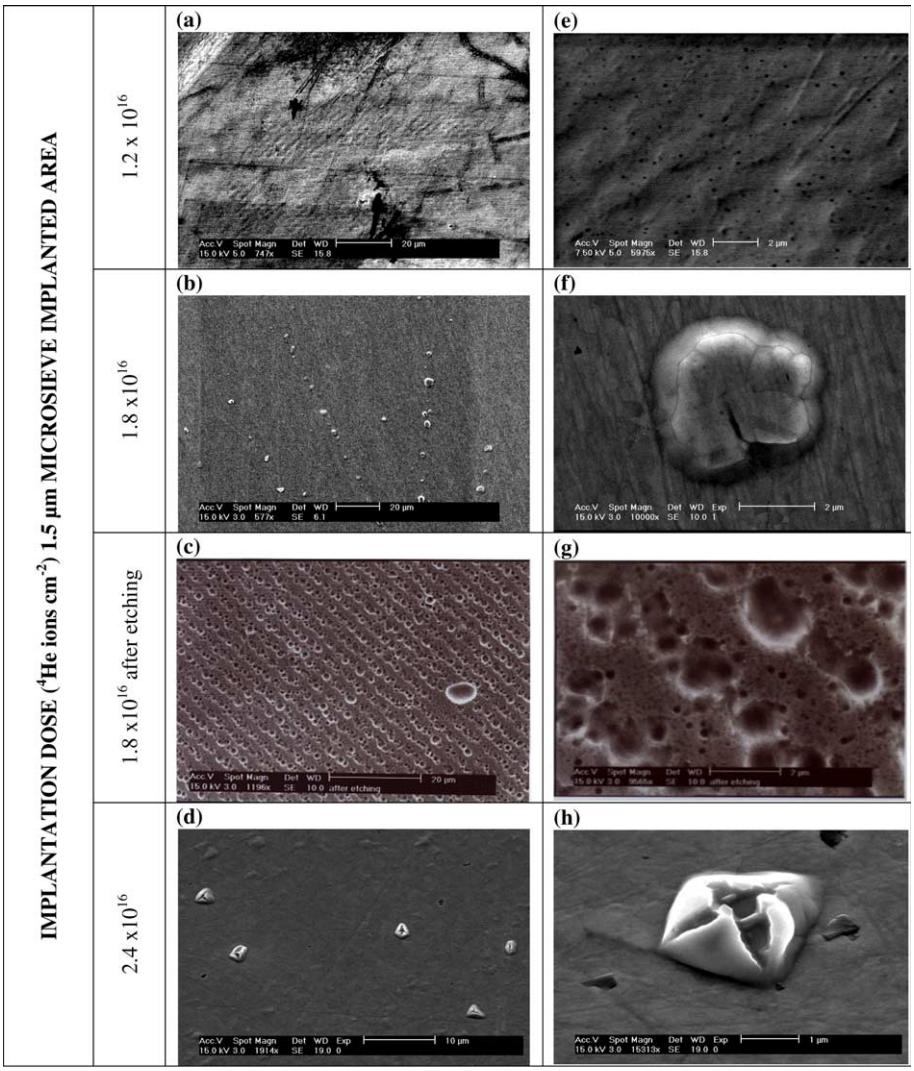

Fig. 6. Selection of SEM pictures obtained from the 1.5 μm microsieve area after implantation at 1.2×10^{16} (a, e), 1.8×10^{16} (b, f) and 2.4×10^{16} (d, h) He ions cm^{-2} and annealing. Pictures (c) and (g) were obtained after electrochemical etching of the sample implanted at 1.8×10^{16} He ions cm^{-2}.

clear that the three different areas studied in this work have produced different results. The one common factor in the results from all three areas summarized in Table 1, must be the helium behaviour. It is therefore worth outlining the aspects of this behaviour that could be relevant. In first place (Section 4.1) we will model theoretically the helium behaviour in terms of bubble coarsening and subsequent swelling. After that in Section 4.2 we will compare the model with the experimental observations and discuss the helium behaviour in the different implantation areas.

4.1. Modeling helium behaviour

As mentioned briefly in the introduction, it is well known that at the end of the implant phase the helium will be present in a high density of small

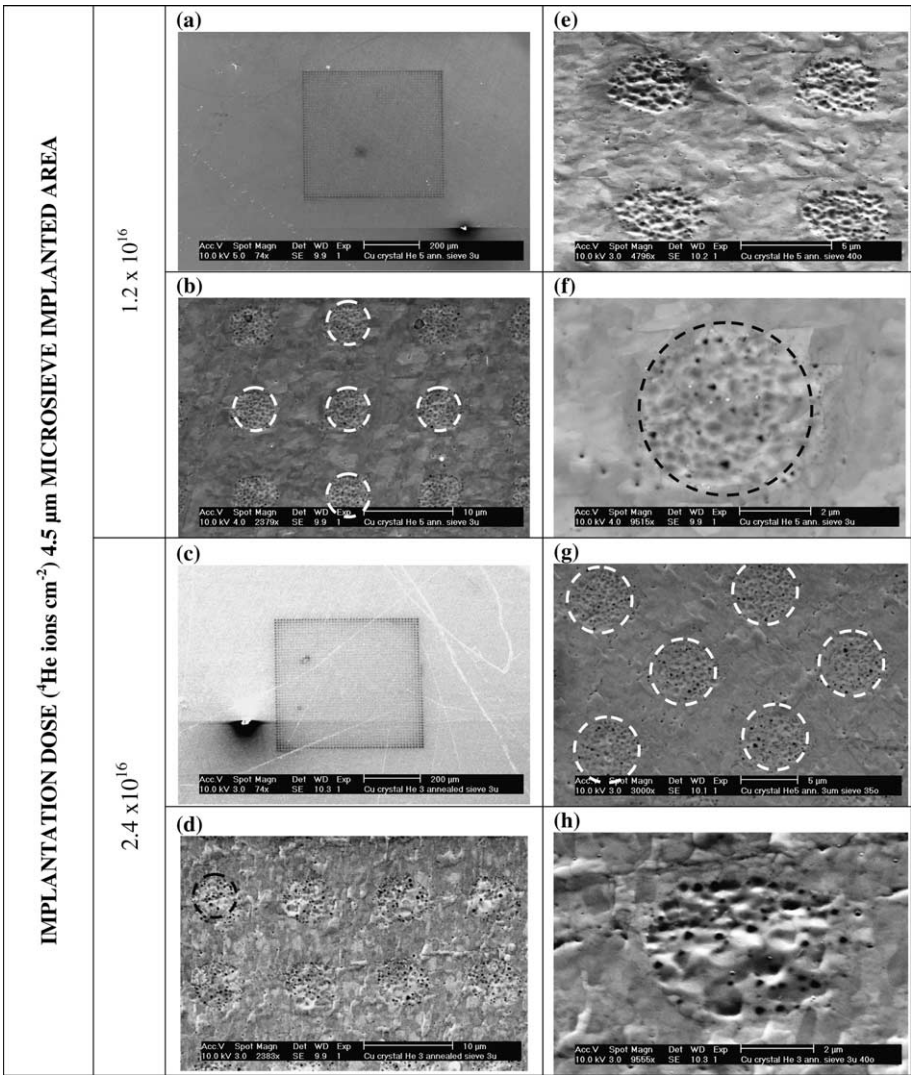

Fig. 7. Selection of SEM pictures obtained from the 4.5 μm microsieve area after implantation at 1.2×10^{16} (a, b, e and f), and 2.4×10^{16} (c, d, g and h) He ions cm^{-2} and annealing. The dotted circles indicate the periodical patches observed after annealing.

bubbles and on annealing towards $0.5T_m$ these small inert gas bubbles become mobile and coalesce, resulting in a coarsening of the bubble substructure and for equilibrium bubbles, a consequent increase in bubble swelling. In copper the coarsening has been directly observed [9,11] as mentioned in the introduction. Ostwald ripening (OR) has also been discussed as a coarsening mechanism, e.g. [16,17]. In the context of the near surface, a further phenomenon, the spatial coarsening effects [16–18] resulting from the flow of thermal vacancies from surfaces may need to be considered. At high gas levels this can lead to the movement of bubbles toward the vacancy source [19]. Some of these effects can be described in more detail.

4.1.1. Coarsening of bubble populations

4.1.1.1. Migration and coalescence. The basic equation governing the rate of coalescence of

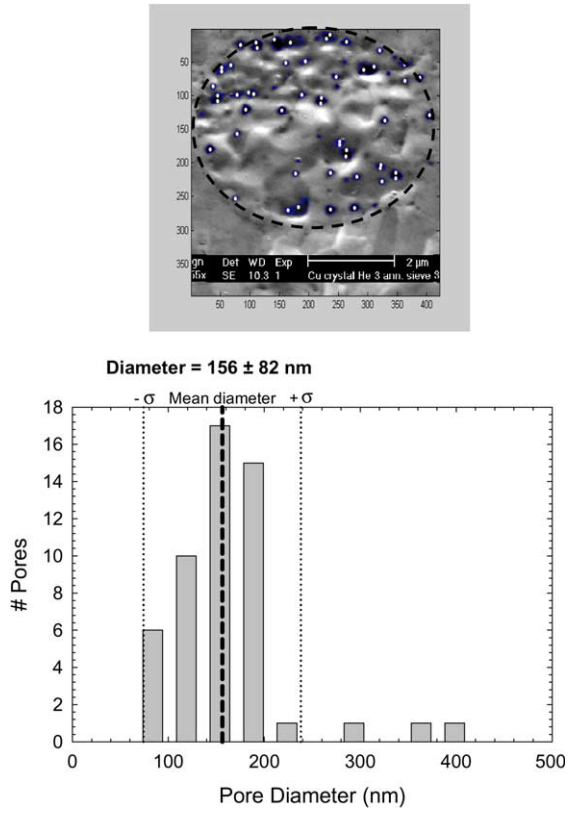

Fig. 8. Diameter distribution of small helium bubbles (black dots) in the 4.5 μm microsieve area after 2.4×10^{16} He ions cm^{-2} implantation and annealing.

randomly migrating particles with radius r_b and volume concentration C_b was first given by Chandrasekhar [20]. In its simplified form, suitable for the applications involving an uniform concentration of bubbles [21], the equation can be written as

$$\frac{dC_b}{dt} = 16\pi D_b r_b C_b^2, \tag{1}$$

where D_b is the bubble diffusivity. It is clear that any coalescence must result in an increase in mean radius. Following the procedures outlined by Goodhew and Tyler [21] this radius, for equilibrium bubbles migrating via surface diffusion in a system annealed at a temperature T for time t, is given by the expression

$$r_b = \left(\frac{45mkT\Omega^{4/3}}{2\pi\gamma} D_s t\right)^{1/5}, \tag{2}$$

where Ω is the atomic volume of the matrix, D_s the surface diffusion coefficient, m the total gas content per unit volume of the host material and the surface energy. This equation is essentially identical to that derived by Gruber [22].

Although the conditions of uniform helium level and available thermal vacancies may limit the applicability of Eq. (2), it seems reasonable to use it to obtain an order of magnitude for the bubble

Table 1
Summary of observations after 973 K annealing of the Cu(1 1 1) crystal as a function of the implantation dose and the implanted area observed

	Implantation dose (ion cm^{-2})		
	1.2×10^{16}	1.8×10^{16}	2.4×10^{16}
Direct implantation	Three-blade, elongated blisters Cracks in the blisters He through bubbles	Faceted balloon-shape[a] blisters After etching: porous structure under the blisters	Faceted dome-shape[b] blisters Decoration of scratches He through bubbles
Microsieve 1.5 μm	Rows of flat blisters Preferential direction	Few big blisters After etching: implanted areas appear	Few broken big blisters
Microsieve 3 μm	Periodical patches[c] No blister formation He through bubbles	–	Periodical patches No blister formation He through bubbles

[a] Balloon-shape: height ~ diameter.
[b] Dome-shape: height > diameter.
[c] Corresponding to the periodical pattern of the microsieve.

size expected from migration and coalescence during annealing. For copper, $\Omega = 1.18 \times 10^{-23}$ cm^3 and we assume $\gamma = 1$ J/m^2. Experimental data for D_s, or rather the effective D_s that might be applied to bubble growth, is sparse but Willertz and Shewmon [23] in their work on helium bubble growth in copper give D_s values deduced from their annealing data. At 975 K they obtained values in the wide range between $\sim 8 \times 10^{-10}$ and 5×10^{-8} cm^2/s, centred on an average value of $\sim 8 \times 10^{-9}$ cm^2/s. It is worth noting that Willertz and Shewman recognized the difficulties of transferring surface diffusion values obtained directed on metal surfaces to the bubble environment. For gold they obtained effective bubble diffusion values some four to five orders of magnitude smaller than expected. The suppression of diffusion mobility of small gas bubbles in solids has been discussed also by Mikhlin [24].

The Ref. [23] values for D_s can be applied using Eq. (2) to the present results where for the highest dose of 2.4×10^{16} cm^{-2}, the peak helium concentration of 1.68 at.% gives a value of $m = 1.42 \times 10^{21}$ atoms cm^{-3}. After a 30-min anneal at 973 K, the calculated bubble radius values using the whole range of D_s values, varied from 8.8 to 20.2 nm with a value of 14.0 nm obtained from the average value for D_s. At the two lower doses, only slightly smaller average values, 12.2 and 13.2 nm, were obtained. It is evident that these values are an order of magnitude smaller that the values observed in the electropolished results. It appears that the observed large cavity sizes cannot be explained by the conventional migration and coalescence mechanism.

4.1.1.2. Ostwald ripening. From the results of Chernikov [17] for copper, the OR mechanism suggests that the mean bubble radius would reach a radius independent of helium level of ~20 nm, again far below the values we are seeking to explain. It might be noted that for similar coarsening results on stainless steel, the OR mechanism was concluded to operate at low helium levels with a transition to migration and coalescence at high helium levels [25]. Since high in this context was of the order of 10^3 appm, it would not be unreasonable to expect migration and coalescence to dominate in the ~1 at.% (10^4 appm) results in the present work.

4.1.2. Bubble swelling

A consequence of the bubble growth is bubble swelling. Under equilibrium condition, even small amounts of inert gas can give rise to significant material swelling if the mean radius is large. At any temperature the relative swelling S (expressed in %) due to inert gas atoms is given simply by the relation

$$S = n_v G, \tag{3}$$

where G is the gas content (at.%) and n_v is the average number of vacancies/gas atom. In turn, we can write that n_v is equal to the atomic density of the host material, ρ_m, divided by the total number of gas atoms/unit volume, ρ_g, i.e.,

$$S = \frac{\rho_m}{\rho_g} G. \tag{4}$$

If we assume for convenience that the ideal gas law $PV = nkT$ is valid and can be rewritten as $P = \rho_g kT$, then the bubble swelling is given by

$$S = \frac{\rho_m r_b kT}{2\gamma} G, \tag{5}$$

hence confirming that for a given temperature and gas level, the key parameter is the (average) gas bubble radius. Applying Eq. (5) to the present annealing of copper at 973 K gives the simple relation

$$S = 0.57 G r_b, \tag{6}$$

with r_b expressed in nanometers.

Using the calculated average radius of 14.0 nm after 30 min annealing, the predicted swelling at the helium peak ($G = 1.68$ at.%) would be 13% (see Fig. 9(b)). The swelling at the helium peak for the lower doses (1.25 and 0.83 at.%) would be 9.4% and 5.8%, respectively. At first sight, these swelling predictions do not appear large enough to be of concern. It should be noted that deviations of the ideal gas law become significant for pressures higher than 100 MPa. The typical pressure for the bubbles considered in this study is 143 MPa ($r = 14.0$ nm) so the calculated swelling from Eqs. (5) and (6) should be taken as a lower limit.

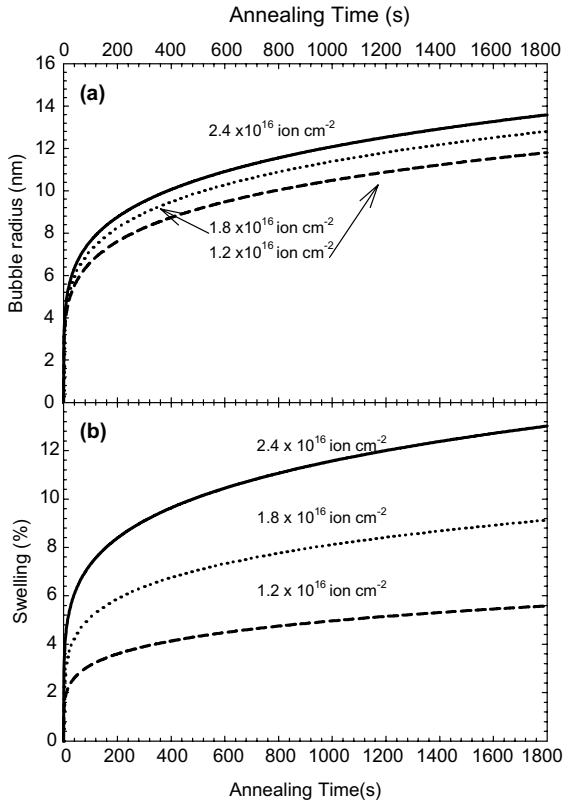

Fig. 9. Theoretical calculation of the helium bubble radius (a) and swelling percentage (b) during annealing at 973 K.

4.1.3. Bubble movement towards the surface

The previous discussions assume that equilibrium bubbles are available uniformly throughout the bubble growth region. However, there is considerable evidence that bubble coarsening initially takes place adjacent to the surface or to grain boundaries [18,26] and is explained by the production of thermal vacancies at these sites. As outlined by Evans and van Veen [19], this phenomenon leads to a significant thermal vacancy gradient which in turn imposes a velocity on bubbles in the gradient towards the vacancy source. In the near surface region where the surface is the primary vacancy source, there is the possibility of significant gas release from bubble movement towards the surface. It was important to check whether this mechanism could account for any part of the very large gas loss observed experimentally. Details will not be given here but the calculation followed identical work on the movement of bubbles in helium implanted nickel [27] but with parameters appropriate to the present work for the highest dose. Although the maximum of the helium concentration present moved some 40 nm towards the surface, only a small amount ($\sim$5%) of helium was released as a result.

4.2. Discussing helium transport on implanted areas

Although there is some confidence that the phenomena of bubble coarsening, swelling and movement will occur, it seems rather difficult from the numbers given in the last section to explain what type of bubble growth could lead to pinhole formation and to the large subsurface bubbles seen after electropolishing, and lead to such a large fraction of helium being released. The major question is why such large bubbles are formed with sizes far greater than the predictions made using conventional bubble migration and coalescence theory.

As a result of this difficulty, the problem was pursued further by carrying out computer simulations of the bubble migration and coalescence processes, using the surface diffusion value already described, and taking into account the depth variation in the implanted helium concentration. The description and results of this work are reported in an accompanying paper [28]. To briefly summarize the results, it seems that at some threshold local swelling, an unexpected breakaway swelling phenomenon was taking place, leading to the formation of very large bubbles centred at the helium peak which grew until they intersected the surface. The bubbles thus had radii of the order of the implanted range and provided an important release route for the gas, leading to the majority of the gas being released. The results of the modeling appear to provide an accurate description of the experimental results in the present work, with the presence of large bubbles, surface pinhole formation, together the large observed gas release.

Besides these general observations relevant to all three different areas studied, each area needs additional comments. To help with the discussion, the bubble behaviour in each area is shown schematically in Fig. 10. Each area can be discussed in turn.

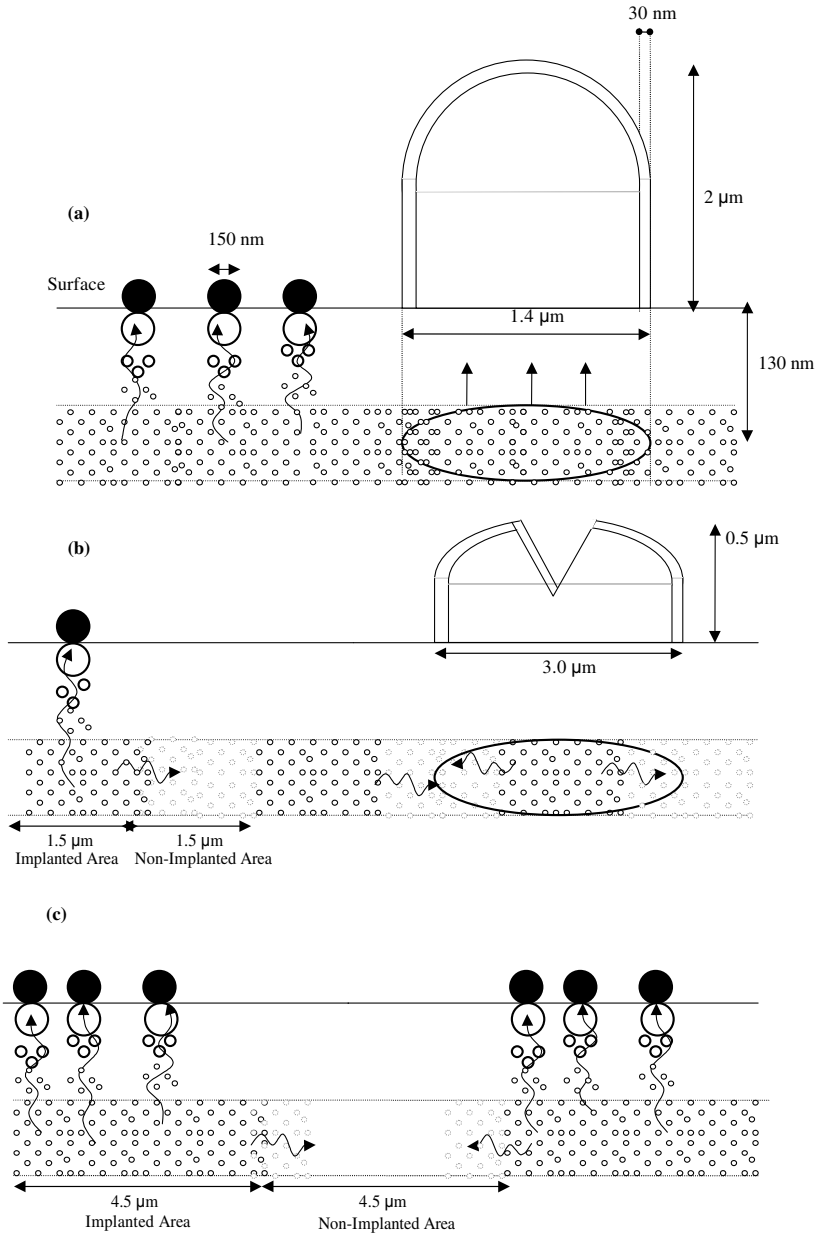

Fig. 10. Sketch of the blister development and helium bubble formation in (a) direct implantation area; (b) 1.5 μm and (c) 4.5 μm microsieve area.

4.2.1. Direct implantation area

In this area, it is clear that protrusions, including the spheroids, were formed, as shown in Fig. 10(a). Basically two types were observed depending on the shape: dome-shape and three-blade shape. Two representative examples are shown in Fig. 4 for the highest implantation dose. The dome-shape spheroid (Fig. 4(a)) has a strongly faceted structure consisting of {1 1 1} and {1 0 0} facets as predicted by the Wulff diagram [29]. The

facets are less clear for the three-blade protrusion (Fig. 4(b)). Cracks appear at the bottom of the blisters indicating that this shape is less favourable to the blister development.

It seems that a few percent of the gas has accumulated in the sub-surface region and has lead to the protrusion formation. An explanation for this formation might be that for large bubbles (0.7 μm radius) the thermal creep induced by the pressure inside the bubble is dominant. As those large bubbles are hardly moving the thermal creep rate is larger than the bubble motion. Bubble surface interactions should then be considered. Once a bubble forms a protrusion it gets underpressurized and wants to shrink to be in thermal equilibrium. Under the expected equilibrium conditions, the pressure under a spheroid is given by $P = 4\gamma/r$ where γ is the surface energy of the copper face. Again using a value of $\gamma = 1$ J/m^2, a helium pressure of 56 bar at 973 K is calculated. The amount of gas in the protrusions, $N_{\mathrm{He}}^{\mathrm{prot}}$ can then be roughly estimated by multiplying the helium density (17 bar RT) times the volume of the protrusions and the areal density of the protrusions:

$$N_{\mathrm{He}}^{\mathrm{prot}} = 17\ \mathrm{bar} \times 3 \times 10^{19}\ \frac{\mathrm{He}}{\mathrm{bar\,cm^3}} \times 3.2 \times 10^{-12}\ \mathrm{cm^3} \times 7 \times 10^{5}\ \mathrm{cm^{-2}} = 1.1 \times 10^{15}\ \mathrm{He\ cm^{-2}}. \quad (7)$$

This figure shows that 5% of the total implanted gas (4.5×10^{15} He cm^{-2} for the highest dose) has lead to the formation of the protrusions. As mentioned above NDP measurements indicated that only 19% of the original gas was still in the samples after the annealing. Therefore there appears to be 14% of the total retained over the original implant depth.

With regard to the observed surface holes, these were estimated to have a diameter of 144 ± 39 nm and a density of 3 dots per μm^2 after image digital analysis (Fig. 5). That means that at a pressure of 267 bar ($P = 2\gamma/r$) approximately 5×10^{15} He ions cm^{-2} escape via those holes. The rest of the implanted helium (60%) has penetrated the surface causing the observed overall surface roughness. In Fig. 11 a branching scheme of the helium behaviour after implantation and subsequent annealing is shown.

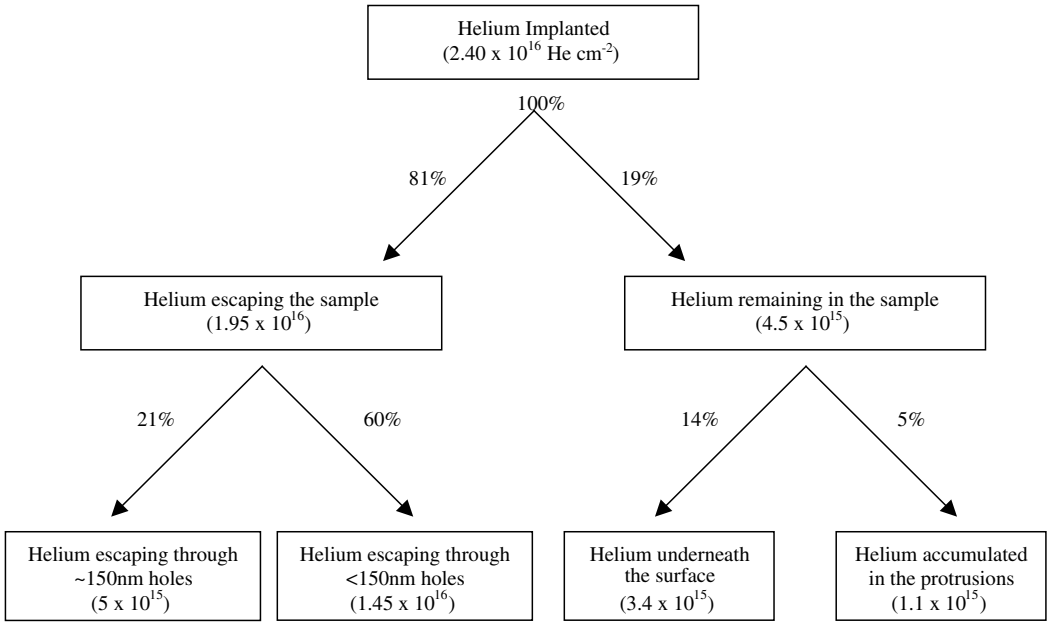

Fig. 11. Branching scheme showing the helium behaviour after implantation and annealing. The numbers between brackets correspond to the highest implantation dose.

4.2.2. 1.5 μm microsieve implantation area

In both the microsieve areas, where there are local implantation areas surrounded by non-damaged material, the situation is more complicated than the direct implant area. A schematic of the behaviour in the 1.5 μm area is shown in Fig. 10(b).

In this area it seems that the distance between pores is short enough to allow the lateral mobility of the implanted helium, and later the small bubbles, to contribute to surface effects. Therefore, the original helium regions defined by the microsieve holes are smeared out at their periphery. This could lead, for example, to the rows of shallow deformations observed in Fig. 6(e). These rows are also seen in the etched samples (c) and (g), where the clear sub-surface bubble images neatly illustrate the results of bubble growth processes. At the highest dose a few big blisters (height 0.5 μm and diameter ~3 μm) appear broken along their axes (Figs. 6(d) and (h)). There is non-deformed material around the implanted zones and, thus, high stresses are exerted during blister development until the break of the protrusions occurs.

4.2.3. 4.5 μm microsieve implantation area

The important result in this area, Fig. 10(c), is that the microsieve periodicity is exactly reflected in the results. It is interesting that no protrusions or spheroids appear. It could be that the total amount of gas in each area is insufficient for their formation. Instead the helium must escape from the sample as small mobile bubbles with a contribution as in other areas from the small holes with a mean diameter of 156 ± 82 nm diameter (see Fig. 8). The retrieval of the periodical pattern of the microsieve makes this process suitable for the study the adhesion of coated samples in a controlled way as will be shown in [30].

5. Conclusions

This work has demonstrated that several different surface effects are seen on copper surfaces after helium implantation to various doses followed by subsequent annealing. An analysis of the underlying helium behaviour was unable to explain the appearance of surface pinholes and large gas release; however, further investigations using computer simulation has led, as described in the following paper [28], to a reasonable understanding of the results. In addition, there are other surface effects such as the development of surface protrusions on copper single crystal surface (1 1 1). At the highest dose, 5% of the implanted helium develops faceted protrusions according to the Wulff diagram. The protrusion formation can be explained in terms of thermal creep of the copper surface. 80% of the implanted helium escapes the sample, 20% via small bubbles of ~145 nm diameter and 60% through smaller bubbles causing an increase of surface roughness.

When the implantations were performed through a periodical microsieve different blistering behaviour is observed. The implantation through a periodical microsieve with 4.5 μm pore size results in periodical patches where helium escapes from the sample without development of protrusions via small bubbles of ~150 nm diameter. The implantation through the small pore size microsieve does not reproduce the periodical pattern and a few broken protrusions appear for the highest dose.

This work has been continued in order to study adhesion of thin films by applying the formation of blisters and gas bubbles in implanted materials [30].

Acknowledgements

This work was financially supported by the Dutch Technology Foundation STW (project number GTF.4901). We wish to thank M.A. van Huis (IRI) for the helium implantation, F. Labohm (IRI) for the NDP measurements, R. van Tijum (RUG) for his help with the image-processing program and H. Bron (RUG) for the electrochemical etching of the samples. We also would like to thank the referee for his very useful comments.

References

[1] H. Dannenberg, J. Appl. Polym. Sci. V (1961) 125.
[2] M.L. Williams, J. Appl. Polym. Sci. 13 (1969) 29.
[3] J. Napolitano, A. Chudnovsky, A. Moet, J. Adhes. Sci. Technol. 2 (1988) 311.

[4] Y.H. Lai, D.A. Dillard, J. Adhes. 31 (1990) 177.
[5] Y.H. Lai, D.A. Dillard, J. Adhes. Sci. Technol. 8 (1994) 663.
[6] Yu.N. Borisenko, V.Y. Gritsyna, T.V. Ivko, J. Adhes. Sci. Technol. 9 (1995) 1413.
[7] A. van Veen, in: S.E. Donnelly, J.H. Evans (Eds.), Fundamental Aspects of Inert Gases in Solids, NATO ASI Series B, Physics, Vol. 279, Plenum Publishing, New York, 1991, p. 41.
[8] D.J. Mazey, B.L. Eyre, J.H. Evans, J. Nucl. Mater. 64 (1977) 145.
[9] P.B. Johnson, D.J. Mazey, Radiat. Eff. 53 (1980) 195.
[10] K.O. Jensen, M. Eldrup, N.J. Pedersen, J.H. Evans, J. Phys. F 18 (1988) 1703.
[11] M.U. Scherzer, Top. Appl. Phys. 52 (1983).
[12] R.G. Downing, G.P. Lamaze, Neutron News 4 (1993) 15.
[13] J.P. Ziegler, J.P. Biersack, U. Littmark, The Stopping and Range of Ions in Solids (TRIM), 1985.
[14] J.H. Evans, R. Williamson, D.S. Whitmell, in: F.A. Garner, J.S. Perrin (Eds.), Effects of Radiation on Materials: Twelfth International Symposium, ASTM STP, Vol. 870, American Society for Testing and Materials, Philadelphia, PA, 1985.
[15] R. van Tijum, Grain recognition of zirconia, Internal Traineeship Applied Physics 0959987, Materials Science Group, Rijksuniversiteit Groningen, 1999.
[16] V.N. Chernikov, H. Trinkaus, P. Jung, H. Ullmaier, J. Nucl. Mater. 170 (1990) 31.
[17] V.N. Chernikov, J. Nucl. Mater. 195 (1992) 29.
[18] N. Marachov, L.J. Perryman, P.J. Goodhew, J. Nucl. Mater. 149 (1987) 296.
[19] J.H. Evans, A. van Veen, J. Nucl. Mater. 233–237 (1996) 1179.
[20] S. Chandrasekhar, Rev. Mod. Phys. 15 (1943) 1.
[21] P.J. Goodhew, S.K. Tyler, Proc. R. Soc. London A 377 (1981) 151.
[22] E.E. Gruber, J. Appl. Phys. 38 (1967) 243.
[23] L.E. Willertz, P.G. Shewmon, Metall. Trans. 1 (1970) 2217.
[24] E.Ya. Mikhlin, Phys. Status Solidi A 56 (1979) 763.
[25] H. Schroeder, P.F.P. Fichtner, H. Trinkaus, in: S.E. Donnelly, J.H. Evans (Eds.), Fundamental Aspects of Inert Gases in Solids, NATO ASI Series B, Physics, Vol. 279, Plenum Publishing, New York, 1991, p. 289.
[26] R.S. Barnes, Philos. Mag. 5 (1960) 635.
[27] J.H. Evans, A. van Veen, J. Nucl. Mater. 252 (1998) 156.
[28] J.H. Evans, R. Escobar Galindo, A. van Veen, Nucl. Instr. and Meth. B, in press. doi:10.1016/j.nimb.2003.10.013.
[29] H. Lüth, Surfaces and Interfaces of Solid Materials, third ed., Springer-Verlag, Berlin, 1995, Chapter 3.
[30] R. Escobar Galindo, A. van Veen, J.H. Evans, H. Schut, J.Th.M. de Hosson, Thin Solid Films, in press.